

# Steerable Conditional Diffusion for Out-of-Distribution Adaptation in Imaging Inverse Problems

Riccardo Barbano<sup>1\*</sup>, Alexander Denker<sup>2\*</sup>, Hyungjin Chung<sup>3\*</sup>, Tae Hoon Roh<sup>4</sup>, Simon Arridge<sup>1</sup>, Peter Maass<sup>2</sup>, Bangti Jin<sup>5</sup>, Jong Chul Ye<sup>3</sup>

<sup>1</sup> Department of Computer Science, University College London

<sup>2</sup> Center for Industrial Mathematics, University of Bremen

<sup>3</sup> Korea Advanced Institute of Science and Technology

<sup>4</sup> Department of Neurosurgery, Ajou University School of Medicine

<sup>5</sup> Department of Mathematics, The Chinese University of Hong Kong  
riccardo.barbano.19@ucl.ac.uk

## Abstract

Denosing diffusion models have emerged as the go-to framework for solving inverse problems in imaging. A critical concern regarding these models is their performance on out-of-distribution (OOD) tasks, which remains an under-explored challenge. Realistic reconstructions inconsistent with the measured data can be generated, hallucinating image features that are uniquely present in the training dataset. To simultaneously enforce data-consistency and leverage data-driven priors, we introduce a novel sampling framework called Steerable Conditional Diffusion. This framework adapts the denoising network specifically to the available measured data. Utilising our proposed method, we achieve substantial enhancements in OOD performance across diverse imaging modalities, advancing the robust deployment of denoising diffusion models in real-world applications.

## 1 Introduction

We consider an image reconstruction task, posed as an inverse problem to recover an image  $\mathbf{x} \in \mathbb{R}^{d_x}$  from measured data  $\mathbf{y} \in \mathbb{R}^{d_y}$  that has undergone a corruption process, formulated as

$$\mathbf{y} = A\mathbf{x} + \boldsymbol{\eta}, \quad (1)$$

with  $A \in \mathbb{R}^{d_y \times d_x}$  being a discrete forward operator. Here we assume the corruption is in the form of additive Gaussian noise  $\boldsymbol{\eta} \sim \mathcal{N}(\mathbf{0}, \sigma_y^2 I_{d_y})$ .

Prior to the advent of deep learning, the recovery of  $\mathbf{x}$  was often recast using variational regularisation,

$$\mathbf{x}^* \in \arg \min_{\mathbf{x} \in \mathbb{R}^{d_x}} \{\mathcal{L}(\mathbf{x}) := \frac{1}{2} \|A\mathbf{x} - \mathbf{y}\|_2^2 + \lambda \mathcal{R}(\mathbf{x})\}, \quad (2)$$

with the first term being the data-fit term, often taken to be the negative log-likelihood of the data, and the second term, weighted by  $\lambda$ , being the regularisation functional. Regularisation is needed due to the ill-posedness of the problem. Several imaging reconstructive tasks can be represented via eq. (1), where the discrete forward transform  $A$  varies with the imaging modality. For instance, Radon transform is used for computed tomography (CT) (Natterer 2001), Fourier transform for magnetic resonance imaging (MRI) (Natterer and Wübbeling 2001), and down-sampling operator for a

super-resolution (SR) task. Analogously, different imaging problems may require ad-hoc regularisation.

Over the past decade, the adoption of deep-learning based solutions has become ubiquitous in the field of image reconstruction, and has significantly transformed the way imaging inverse problems are solved (Arridge et al. 2019). Deep reconstructors, trained on pairs of clean images and measured data, have dominated the scene (Wang, Ye, and Man 2020). Nevertheless, these approaches suffer from inadequate generalisation properties, resulting in subpar performance when applied to out-of-distribution (OOD) reconstructive tasks. Furthermore, they are prone to hallucinating learned image properties or features (Antun et al. 2020). The integration of data-driven methods into clinical practice has been hindered by the shortcomings mentioned above.

In the absence of high-quality paired datasets, some approaches solely learn from measured data, like deep image prior (DIP) (Ulyanov, Vedaldi, and Lempitsky 2018; Baguer, Leuschner, and Schmidt 2020). However, they often underperform compared to supervised deep learned reconstructors on in-distribution tasks. These methods lack the ability to leverage transferable prior information inferred from high-resolution images.

Harnessing data-driven image priors, formulated as generative models, has resulted in significant advances in addressing inverse problems in medical imaging. Diffusion models have shown remarkable abilities in producing high-fidelity images (Song, Meng, and Ermon 2021; Ho, Jain, and Abbeel 2020). Diffusion models, as learned priors from underlying data distributions, can be used within a plug-and-play framework to address a multitude of reconstructive tasks (Zhao, Ye, and Bresler 2023).

Although highly effective in in-distribution reconstructive tasks, diffusion models encounter similar challenges as learned reconstructors when attempting to solve OOD reconstructive tasks. While it has been established that the generalisation capacity of diffusion models is greater than that of supervised-trained deep learning methods (Jalal et al. 2021; Chung and Ye 2022), there is still room for improvement. Generalising to OOD data is crucial when attempting to reconstruct pathologies that are either underrepresented or entirely absent in the training data. Certainly, the scarcity

\* equal contribution.

of available data in medical imaging often necessitates the deployment of learned reconstructors in OOD settings.

Recent attempts to enhance the OOD performance of diffusion models fine-tune a pre-trained diffusion model using a small dataset of ground truth images from the new target domain (Abu-Hussein, Tirer, and Giryes 2022). This line of work shares a similar objective with ours; however, we address a scenario where such a dataset is unavailable. Furthermore, methods have been proposed that aim to train a diffusion model from scratch only given corrupted measured data (Kawar et al. 2023; Daras et al. 2023). Nevertheless, the aforementioned methods require two conditions: i) a large collection of data measurements taken under identical acquisition protocols; and ii) a full rank condition on the imaging operator  $A$  (Daras et al. 2023) or computing its Moore-Penrose pseudo-inverse (Kawar et al. 2023).

In this work, we significantly relax these conditions, as we only require a *single* corrupted measured data, without making any assumptions on the imaging forward operator. To this end, we propose a method, named **Steerable Conditional Diffusion (SCD)**, that guides and constrains the generative process to produce images that are consistent with the measured data  $\mathbf{y}$ . We achieve this by updating the generative process, concurrently with image reconstruction, based solely on the information provided by  $\mathbf{y}$ .

Our contribution can be summarised as follows:

- To our best knowledge, this is the first framework that enables the adaptation of diffusion-based inverse solvers for OOD scenarios, using a single corrupted measured data.
- To streamline the adaptation process, we avoid computationally cumbersome fine-tuning of the pretrained network. Instead, we augment the network with a residual pathway using an efficient low-rank learnable rank decomposition method (Hu et al. 2022).

Finally, our experimental findings show that SCD dramatically enhances the image quality across a variety of real-world, OOD imaging reconstruction problems. This includes  $\mu$ CT, sparse-view medical CT, volumetric CT SR and multi-coil medical MRI. This framework allows for a great flexibility, enabling the utilisation of models pretrained on diverse image distributions.

## 2 Background

### Denoising Diffusion Probabilistic Models

Denoising Diffusion Probabilistic Models (DDPM) (Ho, Jain, and Abbeel 2020; Sohl-Dickstein et al. 2015) model the distribution of interest  $q(\mathbf{x}_0)$  by constructing a parametric hierarchical model  $p(\mathbf{x}_0; \boldsymbol{\theta}) = \int p(\mathbf{x}_T; \boldsymbol{\theta}) \prod_t^T p(\mathbf{x}_{t-1} | \mathbf{x}_t; \boldsymbol{\theta}) d\mathbf{x}_{1:T}$  with latent variables  $\mathbf{x}_{\{1, \dots, T\}} \in \mathbb{R}^{d_x}$  and transition densities  $p(\mathbf{x}_{t-1} | \mathbf{x}_t; \boldsymbol{\theta})$  with learnable parameters  $\boldsymbol{\theta} \in \mathbb{R}^{d_\theta}$ . This defines a  $T$ -length parametrised Markov chain, where transitions are learned to reverse a forward conditional diffusion process  $q(\mathbf{x}_{\{1, \dots, T\}} | \mathbf{x}_0)$ , which gradually adds noise to the data  $\mathbf{x}_0$  using Gaussian conditional transition

kernels defined by

$$\mathbf{x}_t | \mathbf{x}_{t-1} \sim \mathcal{N}(\sqrt{1 - \beta_t} \mathbf{x}_{t-1}, \beta_t I_{d_x}) =: q(\mathbf{x}_t | \mathbf{x}_{t-1}), \quad (3)$$

with forward process variances  $\beta_0 < \dots < \beta_T$  for  $T$  time steps. Here  $\mathbf{x}_0$  is the noiseless image, and  $\mathbf{x}_T$  is a fully corrupted instance drawn from an easy-to-sample noise distribution (e.g., isotropic Gaussian), i.e.,  $\mathbf{x}_T \sim \mathcal{N}(\mathbf{0}, I_{d_x}) =: q(\mathbf{x}_T) = p(\mathbf{x}_T; \boldsymbol{\theta})$ . The forward process admits closed-form sampling of  $\mathbf{x}_t$  conditioned on  $\mathbf{x}_0$  for all  $t \in \{1, \dots, T\}$

$$\mathbf{x}_t | \mathbf{x}_0 \sim \mathcal{N}(\mathbf{x}_t; \sqrt{\bar{\alpha}_t} \mathbf{x}_0, (1 - \bar{\alpha}_t) I_{d_x}) =: q(\mathbf{x}_t | \mathbf{x}_0), \quad (4)$$

with  $\alpha_t = 1 - \beta_t$  and  $\bar{\alpha}_t = \prod_{i=1}^t \alpha_i$  and  $\boldsymbol{\eta} \sim \mathcal{N}(\mathbf{0}, \sigma_y^2 I_{d_y})$ . Training a DDPM amounts to matching the noise  $\boldsymbol{\epsilon} \sim \mathcal{N}(\mathbf{0}, I_{d_x})$  by minimising the so-called  $\epsilon$ -matching objective

$$\min_{\boldsymbol{\theta} \in \mathbb{R}^{d_\theta}} \mathbb{E}_{t \in U\{0, T\}, \mathbf{x}_0 \sim q(\mathbf{x}_0), \boldsymbol{\epsilon} \sim \mathcal{N}(\mathbf{0}, I_{d_x})} [\|\boldsymbol{\epsilon}(\mathbf{x}_t, t; \boldsymbol{\theta}) - \boldsymbol{\epsilon}\|_2^2],$$

where we write  $\mathbf{x}_t$  as a linear combination of  $\mathbf{x}_0$  and the noise  $\boldsymbol{\epsilon}$ , i.e.,  $\mathbf{x}_t = \sqrt{\bar{\alpha}_t} \mathbf{x}_0 + \sqrt{1 - \bar{\alpha}_t} \boldsymbol{\epsilon}$ . Moreover, via the  $\epsilon$ -matching objective a multi-noise level residual denoiser  $\boldsymbol{\epsilon}(\mathbf{x}_t, t; \boldsymbol{\theta})$  is learned as a proxy for the (Stein) score, i.e.,  $\nabla_{\mathbf{x}} [\log q](\mathbf{x}_t) \approx -\boldsymbol{\epsilon}(\mathbf{x}_t, t; \boldsymbol{\theta}^*) / \sqrt{1 - \bar{\alpha}_t} =: \mathbf{s}(\mathbf{x}_t, t; \boldsymbol{\theta}^*)$  (Song et al. 2020) with  $\boldsymbol{\theta}^*$  being a minimiser of the  $\epsilon$ -matching objective. Note that  $\nabla_{\mathbf{x}} [\log q](\mathbf{x}_t)$  is the gradient of the log-density of interest with respect to the first argument, evaluated at  $\mathbf{x}_t$ . Training a DDPM also implies learning the score  $\mathbf{s}(\mathbf{x}_t, t; \boldsymbol{\theta})$ . The denoiser is trained such that the generative process  $p(\mathbf{x}_{\{1, \dots, T\}}; \boldsymbol{\theta}^*)$  approximates well the intractable reverse process for all  $t$ , i.e.,  $p(\mathbf{x}_{t-1} | \mathbf{x}_t; \boldsymbol{\theta}^*) \approx q(\mathbf{x}_{t-1} | \mathbf{x}_t)$ . The reverse diffusion process ends with  $\mathbf{x}_0$  by iteratively denoising a sequence of noisy samples starting from pure noise  $\mathbf{x}_T \sim \mathcal{N}(\mathbf{0}, I_{d_x})$ . Initially, ancestral sampling was adopted by (Ho, Jain, and Abbeel 2020) for solving the reverse process.

### Diffusion Models in Imaging Problems

In imaging inverse problem, there is additional conditioning information  $\mathbf{y}$ , associated to  $\mathbf{x}_0$  via eq. (1). The recovery of  $\mathbf{x}_0$  is then conditioned on  $\mathbf{y}$ , as one aims to embed  $\mathbf{y}$  via the posterior distribution of  $\mathbf{x}_t | \mathbf{y}$ , or equivalently via its score:

$$\nabla_{\mathbf{x}} [\log p(\cdot | \mathbf{y})](\mathbf{x}_t) = \nabla_{\mathbf{x}} [\log p](\mathbf{x}_t) + \nabla_{\mathbf{x}} [\log p(\mathbf{y} | \cdot)](\mathbf{x}_t).$$

Note that the prior score is learned, and thus approximated as  $\mathbf{s}(\mathbf{x}_t, t; \boldsymbol{\theta})$ , while  $p(\mathbf{y} | \mathbf{x}_t) = \int p(\mathbf{y} | \mathbf{x}_t) p(\mathbf{x}_0 | \mathbf{x}_t) d\mathbf{x}_0$ , under the conditional independence assumption that  $\mathbf{x}_0 \perp\!\!\!\perp \mathbf{y} | \mathbf{x}_t$ . The main difficulty is that the likelihood score is only accessible at  $t = 0$ . To circumvent this issue, different strategies have been proposed (Song et al. 2020; Jalal et al. 2021; Chung and Ye 2022; Liu et al. 2023; Wu et al. 2023). We adopt the solution due to (Chung et al. 2023a)

$$p(\mathbf{y} | \mathbf{x}_t) \approx p(\mathbf{y} | \hat{\mathbf{x}}_0), \quad \text{with } \hat{\mathbf{x}}_0 := \mathbb{E}[\mathbf{x}_0 | \mathbf{x}_t], \quad (5)$$

where the posterior mean  $\mathbb{E}[\mathbf{x}_0 | \mathbf{x}_t]$  is obtained in closed-form via Tweedie's approach (Efron 2011; Kim and Ye 2021). Recently, (Chung, Lee, and Ye 2023) propose a very promising sampling scheme building on one of the most widely acknowledged accelerated diffusion sampling strategies, i.e., denoising diffusion implicit model (DDIM) (Song,

Meng, and Ermon 2021). Following DDIM, one can generate a sample  $\mathbf{x}_{t-1}$  from a sample  $\mathbf{x}_t$  via,

$$\mathbf{x}_{t-1} = \sqrt{\bar{\alpha}_t} \hat{\mathbf{x}}_0(\mathbf{x}_t; \boldsymbol{\theta}^*) + \sqrt{1 - \bar{\alpha}_{t-1} - \eta_t^2} \boldsymbol{\epsilon}(\mathbf{x}_t, t; \boldsymbol{\theta}^*) + \eta_t \boldsymbol{\epsilon},$$

where we use  $\eta_t = \eta \sqrt{(1 - \bar{\alpha}_{t-1}) / (1 - \bar{\alpha}_t)} \sqrt{1 - \bar{\alpha}_t / \bar{\alpha}_{t-1}}$  and  $\hat{\mathbf{x}}_0(\mathbf{x}_t; \boldsymbol{\theta}^*)$  is given by Tweedie’s formula, i.e.,

$$\hat{\mathbf{x}}_0(\mathbf{x}_t; \boldsymbol{\theta}^*) = (\mathbf{x}_t - \sqrt{1 - \bar{\alpha}_t} \boldsymbol{\epsilon}(\mathbf{x}_t, t; \boldsymbol{\theta}^*)) / \sqrt{\bar{\alpha}_t}. \quad (6)$$

The right-hand side (RHS) of the DDIM update rule consists of three components: the predicted de-noised image, the deterministic noise component, and the stochastic noise component (from left to right). (Chung, Lee, and Ye 2023) present Decompose Diffusion Sampling (DDS), which incorporates within the denoising step, a data consistency step, which does not require backpropagating through the network as in (Chung et al. 2023a). Thus,  $\hat{\mathbf{x}}_0$  is replaced by  $\hat{\mathbf{x}}'_0(\mathbf{x}_t; \boldsymbol{\theta}^*) = \text{CG}^{(p)}(\hat{\mathbf{x}}_0(\mathbf{x}_t; \boldsymbol{\theta}^*))$ , where CG takes  $p$  conjugate gradient steps with respect to the negative log-density of the measured data defined by eq. (1). To simplify the notation, we omit the dependence on  $\mathbf{x}_t$  and  $\boldsymbol{\theta}$  where it is not necessary, in  $\hat{\mathbf{x}}_0$  and  $\hat{\mathbf{x}}'_0$ .

### 3 Steerable Conditional Diffusion

The proposed approach, called Steerable Conditional Diffusion (SCD) sampling, focuses on tuning the learned denoiser network, i.e., a U-Net, in the reverse diffusion process solely based on the conditioning variable  $\mathbf{y}$ . Data consistency is crucial when the image to be recovered, denoted as  $\mathbf{x}$ , is sampled from a distribution of interest  $\tilde{q}(\mathbf{x})$  that mildly (or severely) deviates from the distribution  $q(\mathbf{x}_0)$  used at training. SCD mitigates the effect of covariate shift (Tran, Snoek, and Lakshminarayanan 2020), i.e.,  $q(\mathbf{x}) \neq \tilde{q}(\mathbf{x})$ . To control the generative process to create images that are consistent with  $\mathbf{y}$ , and avoid hallucinating image features that are inconsistent with the measured data, the denoiser network is further parametrised by an additional learnable pathway injected at an architectural level. At generation-time, each U-Net’s convolutional operation is equipped with a new residual pathway uniquely learned via the measured data  $\mathbf{y}$ , while keeping backbone convolutional parameters frozen. The SCD pseudo-code is in Algorithm 1 and the details are as follows.

#### Generation-Time Adjustable Parameters Injection

At generation-time, SCD samples from the reverse diffusion process, augmenting each convolutional layer in  $\boldsymbol{\epsilon}(\cdot; \boldsymbol{\theta}^*)$  with learnable rank decomposition matrices via Low Rank (LoRA) injection (Hu et al. 2022). Given a learned matrix  $W \in \mathbb{R}^{m \times n}$ , which represents a convolutional operation within  $D$  convolutional layers in  $\boldsymbol{\epsilon}(\cdot; \boldsymbol{\theta}^*)$ , the LoRA injection re-writes  $W$  as

$$\tilde{W} = W + \Delta W, \quad \text{with } \Delta W = AB^\top, \quad (7)$$

where  $A \in \mathbb{R}^{m \times r}$ ,  $B \in \mathbb{R}^{n \times r}$  form a low-rank approximation to the residual update  $\Delta W$ , i.e.,  $r \ll \min(m, n)$ . In practice,  $A$  is randomly initialised such that all the entries are draws from a standard Gaussian, while  $B$  is set to a zero

---

#### Algorithm 1: SCD

---

**Inputs:** U-Net  $\boldsymbol{\epsilon}(\cdot; \boldsymbol{\theta}^*)$ , initial  $\mathbf{x}_T$ , measured data  $\mathbf{y}$ , number of sampling steps  $T$ , adaptation objective  $\mathcal{L}$ , number of optim. steps  $K$ , data-consistency function  $\Gamma$

```

1 Function inject_LoRA ( $\boldsymbol{\epsilon}(\cdot; \boldsymbol{\theta}^*)$ ):
   /* based on (Hu et al. 2022) */
2   return  $\boldsymbol{\epsilon}(\cdot; \boldsymbol{\theta}^*, \Delta\boldsymbol{\theta})$ 

3 Function adapt ( $\mathbf{x}_t, \mathbf{y}, \Gamma$ ):
4   for  $k = 1, \dots, K$  do
5      $\boldsymbol{\epsilon}_t \leftarrow \boldsymbol{\epsilon}(\mathbf{x}_t, t; \boldsymbol{\theta}^*, \Delta\boldsymbol{\theta}_{k-1})$ 
6      $\hat{\mathbf{x}}_0 \leftarrow (\mathbf{x}_t - \sqrt{1 - \bar{\alpha}_t} \hat{\boldsymbol{\epsilon}}_t) / \sqrt{\bar{\alpha}_t}$  // denoising
7      $\hat{\mathbf{x}}'_0 \leftarrow \Gamma(\mathbf{y}, \mathbf{x}_t)$  // data-consistency
8      $\Delta\boldsymbol{\theta}_k \leftarrow \Delta\boldsymbol{\theta}_{k-1} - \text{AdamGrad}(\mathcal{L}(\Delta\boldsymbol{\theta}))$ 
9   end

10  $\boldsymbol{\epsilon}(\cdot; \boldsymbol{\theta}^*, \Delta\boldsymbol{\theta}) \leftarrow \text{inject\_LoRA}(\boldsymbol{\epsilon}(\cdot; \boldsymbol{\theta}^*))$ 
11 for  $t = T, \dots, 1$  do
12    $\boldsymbol{\epsilon}_t^{\text{DDIM}} \leftarrow \boldsymbol{\epsilon}(\mathbf{x}_t, t; \boldsymbol{\theta}^*)$ 
13    $\text{adapt}(\mathbf{x}_t, \mathbf{y}, \Gamma)$ 
14    $\boldsymbol{\epsilon}_t \leftarrow \boldsymbol{\epsilon}(\mathbf{x}_t, t; \boldsymbol{\theta}^*, \Delta\boldsymbol{\theta}_t^*)$ 
15    $\hat{\mathbf{x}}_0 \leftarrow (\mathbf{x}_t - \sqrt{1 - \bar{\alpha}_t} \boldsymbol{\epsilon}_t) / \sqrt{\bar{\alpha}_t}$  // adjusted estimate
16    $\hat{\mathbf{x}}'_0 \leftarrow \Gamma(\mathbf{y}, \mathbf{x}_t)$ 
17    $\boldsymbol{\epsilon} \sim \mathcal{N}(\mathbf{0}, I_{d_x})$ 
18    $\mathbf{x}_{t-1} \leftarrow \sqrt{\bar{\alpha}_t} \hat{\mathbf{x}}'_0 + \sqrt{1 - \bar{\alpha}_{t-1} - \eta_t^2} \boldsymbol{\epsilon}_t^{\text{DDIM}} + \eta_t \boldsymbol{\epsilon}$ 
19 end
Output:  $\hat{\mathbf{x}}_0$ 

```

---

matrix, i.e., at  $t = 0$  we have  $AB^\top = \mathbf{0}$ . Note that LoRA injection is utilised; however, SCD is also adaptable to incorporate alternative fine-tuning strategies. We then refer to  $\Delta\boldsymbol{\theta}$  as a vector obtained by stacking vectorised elements of  $(\Delta W_d | \Delta W_d^\top)_{d=1}^D$ .

The adaptation procedure is outlined in Algorithm 1, i.e., lines 3-9. To condition the de-noised posterior mean on  $\mathbf{y}$ , SCD uses the results from (Ravula et al. 2023),

$$\mathbb{E}[\mathbf{x}_0 | \mathbf{x}_t, \mathbf{y}] = \frac{1}{\sqrt{\bar{\alpha}_t}} (\mathbf{x}_t + (1 - \bar{\alpha}_t) \nabla_{\mathbf{x}} [\log p(\cdot | \mathbf{y})](\mathbf{x}_t)),$$

with the RHS factorised as

$$\frac{1}{\sqrt{\bar{\alpha}_t}} (\mathbf{x}_t + (1 - \bar{\alpha}_t) (\nabla_{\mathbf{x}} [\log p](\mathbf{x}_t) + \nabla_{\mathbf{x}} [\log p(\mathbf{y} | \cdot)](\mathbf{x}_t))).$$

For the gradient of the prior, we use the plug-in approximation. Recall that  $\nabla_{\mathbf{x}} [\log p](\mathbf{x}_t) \approx \mathbf{s}(\mathbf{x}_t, t; \boldsymbol{\theta}^*, \Delta\boldsymbol{\theta}) := -\boldsymbol{\epsilon}(\mathbf{x}_t, t; \boldsymbol{\theta}^*, \Delta\boldsymbol{\theta}) / \sqrt{1 - \bar{\alpha}_t}$ , where this relationship between the score-matching and  $\boldsymbol{\epsilon}$ -matching parametrisation can be found in (Song et al. 2020). For the gradient of the likelihood, we propose to approximate as

$$\begin{aligned} \nabla_{\mathbf{x}} [\log p(\mathbf{y} | \cdot)](\mathbf{x}_t) &\approx \frac{-1}{2\sigma_y^2(1 - \bar{\alpha}_t)} \nabla_{\mathbf{x}} [\|A\hat{\mathbf{x}}_0 - \mathbf{y}\|_2^2](\mathbf{x}_t) \\ &\approx \frac{-\sqrt{\bar{\alpha}_t}}{2\sigma_y^2(1 - \bar{\alpha}_t)} \nabla_{\mathbf{x}} [\|A\hat{\mathbf{x}}_0 - \mathbf{y}\|_2^2](\hat{\mathbf{x}}_0) \end{aligned}$$

where the first approximation is given by (Chung et al. 2023a), while the second approximation is similar to what

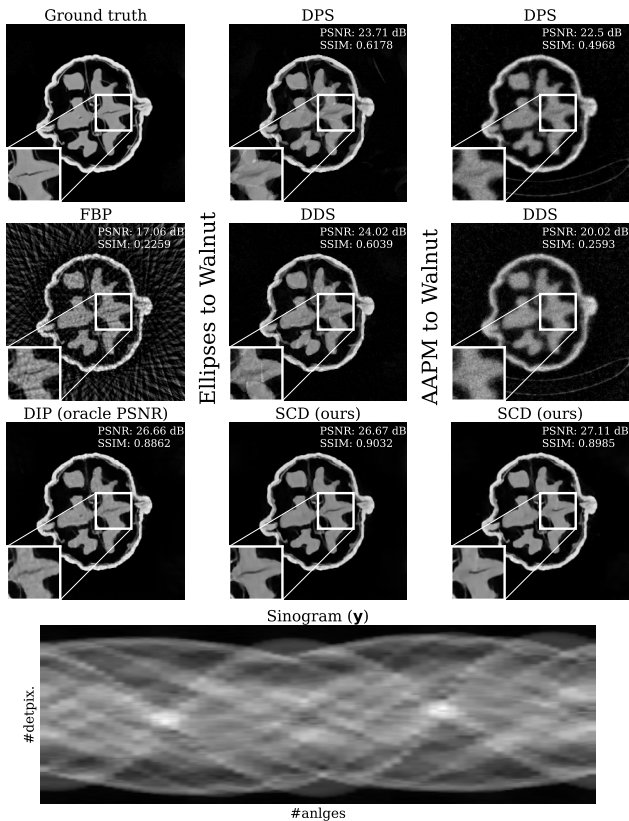


Figure 1: DPS, DDS, SCD (ours), and the DIP are compared to reconstruct real-measured  $\mu$ CT data of a walnut from 60 angles and 128 detector pixels. The measured data, called Sinogram, is also shown (bottom).

is used in (Chung, Lee, and Ye 2023; Chung, Kim, and Ye 2023). Notably, the second essentially approximates the Jacobian of the network, i.e.,  $\partial_{\mathbf{x}_t} \epsilon(\mathbf{x}_t, t; \theta^*)$ , to be the identity, saving us from cumbersome computations. In a different application, this last approximation is widely used (Poole et al. 2023), as the Jacobian incorporation is known to be notoriously unstable (Du et al. 2023; Salimans and Ho 2021). Thus, Tweedie estimate conditioned on  $\mathbf{y}$  is

$$\mathbb{E}[\mathbf{x}_0 | \mathbf{x}_t, \mathbf{y}] \approx \hat{\mathbf{x}}_0 - \gamma A^\top (A\hat{\mathbf{x}}_0 - \mathbf{y}) =: \hat{\mathbf{x}}'_0. \quad (8)$$

See Appendix C for additional clarification on the approximation. In Algorithm 1 line 7 and line 16,  $\Gamma$  represents a function moving towards the minimiser of the negative log-density of interest, such as one or more steps of gradient descent or CG; it thus plays the role of an (approximate) data-consistency projection. SCD further parametrises  $\hat{\mathbf{x}}'_0$  with respect to the residual  $\Delta\theta$ , while keeping  $\theta$  frozen. The residual  $\Delta\theta$  is then updated based on  $\hat{\mathbf{x}}'_0$  as per line 8 in Algorithm 1. The update is recast as minimising the objective:

$$\Delta\theta^* \in \arg \min_{\Delta\theta} \{\mathcal{L}(\Delta\theta) := \|A\hat{\mathbf{x}}'_0 - \mathbf{y}\|_2^2\}, \quad (9)$$

with  $\hat{\mathbf{x}}'_0$  depending on  $\Delta\theta$ . In a similar spirit to eq. (2), a regularisation functional  $\mathcal{R} : \mathbb{R}^{d_x} \rightarrow \mathbb{R}_+$ , weighted by a scalar

$\lambda$ , can be included in eq. (9). Overall, the `adapt` routine (line 9) aims to minimise the above objective by learning the residual  $\Delta\theta$  to adapt the OOD nature of the problem, where AdamGrad are the gradients computed using Adam (Kingma and Ba 2015). This objective is evaluated on the de-noised conditional mean at each sampling step  $t$ .

## Sampling from Adjustable Generative Process

The reverse sampling intertwines the DDIM update rule with the above adaptation step. SCD’s update rule is reported in Algorithm 1, see lines 11-18. Note that the augmented network, i.e.,  $\epsilon(\cdot; \theta^*, \Delta\theta)$  is only used for the predicted de-noised estimate  $\mathbf{x}_0$ , while the deterministic noise update uses  $\epsilon(\cdot; \theta^*)$ . This is to avoid the “de-naturalisation” of  $\epsilon(\cdot; \theta^*)$  to act as a multi-noise level denoiser due to the adjustable parameters injection being learned to solve a reconstructive task. This designing choice arises as a logical outcome of the proposed methods, where the log prior score is augmented with a residual architectural pathway. This pathway adjusts the score according to  $\mathbf{y}$ , ensuring that  $\hat{\mathbf{x}}'_0$  maintains a high level of consistency with the measured data  $\mathbf{y}$ .

## 4 Multi-modality Reconstruction Tasks

Our empirical evaluation of the proposed method encompasses two of the most popular imaging modalities in clinical practice (Natterer 2001): CT and MRI. For CT we conduct two experimental investigations: a sparse-view CT reconstruction and volumetric SR. The volumetric CT SR task uses in-vivo collected data. It’s important to highlight that SR possesses distinct characteristics compared to the other two tasks, as the former tasks are categorised as reconstructive, while SR is primarily a restoration task. Furthermore, due to the volumetric nature of CT SR, we apply the diffusion model independently to each slice. For MRI, we consider accelerated multi-coil medical MRI.

**Sparse-view Computed Tomography** Models are trained on both the publicly released dataset for the American Association of Physicists in Medicine (AAPM) grand challenge (Moen et al. 2021), and a synthetic ELLIPSES dataset (Adler and Öktem 2018). The training specifics follow the identical setting as in (Chung, Lee, and Ye 2023; Dhariwal and Nichol 2021). The AAPM dataset comprises 3839 images, resized to  $256 \times 256$  resolution. The ELLIPSES dataset consists of images of a varying number of ellipses at different positions and orientations. For a detailed description of all used datasets, we refer to Appendix A. To evaluate the OOD performance of DDPM-based baselines compared to SCD, we use two additional datasets: the LODOPAB-CT (Leuschner et al. 2021) dataset and a real-measured one, i.e., the WALNUT (Der Sarkissian et al. 2019) dataset. The LODOPAB-CT dataset comprises thoracic CT images resized to  $256 \times 256$ . We rotate the images to match the anatomical orientation of AAPM, so that it serves as a mild-ODD example for AAPM. For the AAPM, ELLIPSES, and LODOPAB-CT datasets, the measured data is simulated via a parallel-beam geometry using 60 equidistant angles, and 1% relative Gaussian noise is added. The WALNUT dataset comprises a real-measured  $\mu$ CT of a walnut, and its data,

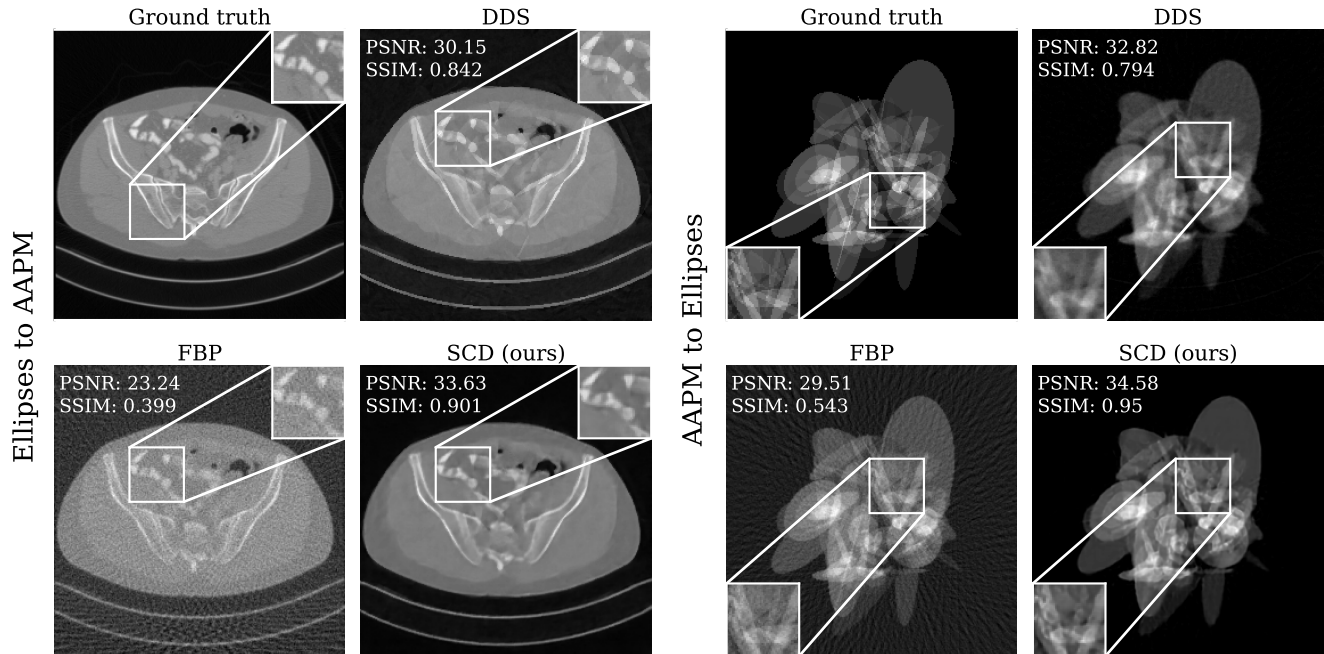


Figure 2: Results for sparse view CT. We test two settings: training on ELLIPSES and testing on AAPM, and training on AAPM and testing on ELLIPSES. As a classical baseline, we also show the FBP reconstruction.

	$q(\mathbf{x}_0)$	$\tilde{q}(\mathbf{x}_0)$	DDS		SCD	
			PSNR	SSIM	PSNR	SSIM
SPARSE VIEW CT	AAPM	AAPM	39.55 $\pm$ 0.08	0.951 $\pm$ 0.001	39.77 $\pm$ 0.07	0.952 $\pm$ 0.001
		LoDOPAB	31.20 $\pm$ 0.21	0.742 $\pm$ 0.007	33.88 $\pm$ 0.28	0.865 $\pm$ 0.008
		ELLIPSES	33.11 $\pm$ 0.11	0.787 $\pm$ 0.005	35.55 $\pm$ 0.10	0.958 $\pm$ 0.001
	ELLIPSES	ELLIPSES	36.91 $\pm$ 0.09	0.972 $\pm$ 0.001	36.32 $\pm$ 0.09	0.969 $\pm$ 0.000
		AAPM	30.82 $\pm$ 0.06	0.847 $\pm$ 0.002	34.21 $\pm$ 0.12	0.890 $\pm$ 0.001
		LoDOPAB	31.80 $\pm$ 0.22	0.798 $\pm$ 0.009	33.85 $\pm$ 0.24	0.845 $\pm$ 0.007
ACCELERATED MRI	BRAIN	BRAIN	30.34 $\pm$ 0.15	0.810 $\pm$ 0.006	30.47 $\pm$ 0.15	0.815 $\pm$ 0.005
		KNEE	29.47 $\pm$ 0.15	0.738 $\pm$ 0.004	30.31 $\pm$ 0.16	0.757 $\pm$ 0.005
	KNEE	KNEE	31.02 $\pm$ 0.17	0.777 $\pm$ 0.005	31.10 $\pm$ 0.17	0.778 $\pm$ 0.005
		BRAIN	28.62 $\pm$ 0.17	0.773 $\pm$ 0.005	28.85 $\pm$ 0.18	0.780 $\pm$ 0.005

Table 1: PSNR and SSIM (mean  $\pm$  SE) for DDS vs. SCD on sparse-view CT and accelerated MRI.

collected using a cone-beam scanner, is also sub-sampled to 60 angles. For more technical information on the data simulation, such as the acquisition geometries, please refer to Appendix A. For the sparse-view CT reconstructions, we include the total variation (TV) as the additional regulariser in eq. (9), i.e.,  $\mathcal{R}(\mathbf{x}) = \text{TV}(\mathbf{x})$  (Rudin, Osher, and Fatemi 1992).

**Accelerated MRI** We train diffusion models on the KNEE/BRAIN multi-coil fastMRI (Zbontar et al. 2018) datasets. For the KNEE dataset, we follow a similar setting to (Chung, Lee, and Ye 2023) and consider 973 volumes for training. Similarly, for models trained on BRAIN, we use 3842 patient volumes. To simulate the data with a uni-

form 1D sub-sampling ( $\times 4$  acceleration) and an 8% Auto Calibrating Signal (ACS) region, we follow the original setting proposed in (Zbontar et al. 2018). Additionally, we add 1% relative Gaussian noise to the measured data. The coil sensitivity maps are pre-estimated using ESPIRiT (Uecker et al. 2014). Following (Jalal et al. 2021; Chung, Lee, and Ye 2023), we use the minimum variance unbiased estimate (MVUE) images as our ground truth. Evaluation is conducted on 10 held-out test volumes for the KNEE, and 18 held-out test volumes for the BRAIN.

**Super-resolution** For this task, novel real-measured data has been collected:  $\mu$ CT of the head of a pig with a re-

duced field-of-view (FOV), imaging the interior with a very high resolution of  $0.1 \text{ mm}^3$ . To evaluate SCD, a 5mm coarse-vertical-resolution multi-detector computed tomography (MDCT) (Kalra et al. 2004) scan of the head of a pig is also collected. The objective is to enhance the vertical resolution to achieve isotropic resolution as much as possible. The problem is formulated as  $\times 8$  SR on the  $z$ -axis. The two datasets present vastly different image features and statistics, including different contrast levels. For more details, we refer to Appendix A.

## 5 Results and Discussion

Our experimental session follows the following rationale. We first benchmark SCD against DPS (Chung et al. 2023a) and DDS on a reconstructive task from real-measured sparse-view  $\mu$ CT data of a walnut. We then conduct extensive analysis on reconstructive tasks from sparse-view CT data and accelerated multi-coil MRI data. We also include a volumetric SR task based on a novel MDCT dataset.

### Initial Evaluation on $\mu$ CT Walnut Data

We evaluate DPS, DDS, and SCD using models trained on both AAPM and ELLIPSES datasets, reconstructing the  $\mu$ CT data using only 60 angles. Figure 1 reports the reconstruction for each method along with PSNR/SSIM values, as well as exemplifying hallucinatory behaviours of the state-of-the-art diffusion sampling schemes. When using DPS or DDS, models trained on the ELLIPSES dataset lead to stronger artefacts (or hallucinations) compared to AAPM trained ones. Small ellipses are clearly visible in the reconstructed walnut. However, models trained on the AAPM dataset also hallucinates a white bow below the walnut which is indeed not part of the ground truth image. SCD instead results in a robust recovery of the walnut no matter if the model had been trained on ELLIPSES or the AAPM dataset. As expected from (Chung, Lee, and Ye 2023), DDS shows better performance compared to DPS, and it is also the most robust in medical imaging settings where the forward operator is global. We further compared DPS vs. DDS in an in-distribution task where DDS consistently outperformed DPS: ELLIPSES  $\rightarrow$  ELLIPSES results in 31.34dB vs. 36.91dB, and AAPM  $\rightarrow$  AAPM: 38.38dB vs. 39.55dB. Henceforth, SCD is only benchmarked against DDS. We also include a DIP approach (Ulyanov, Vedaldi, and Lempitsky 2018), an unsupervised generative method (Dimakis 2022). DIP is well-known to be prone to overfitting, thus we early stop based on the highest PSNR obtained in the optimisation process, i.e., reporting an oracle PSNR. Overall, SCD shows better performance, along with visual quality.

**Ablation:**  $\mathbb{E}[\mathbf{x}_0|\mathbf{x}_t]$  vs.  $\mathbb{E}[\mathbf{x}_0|\mathbf{x}_t, \mathbf{y}]$  Our method builds upon the conditional Tweedie estimate, i.e.,  $\mathbb{E}[\mathbf{x}_0|\mathbf{x}_t, \mathbf{y}]$ . We benchmark against a variant of SCD, where only the unconditional Tweedie estimate, i.e.,  $\hat{\mathbf{x}}_0 \approx \mathbb{E}[\mathbf{x}_0|\mathbf{x}_t]$ , is used. Note that this corresponds to removing line 7 and line 16 from the Algorithm 1. By doing so, we only exploit the measured data in `adapt`, i.e., line 8. In `adapt`, the minimisation of  $\mathcal{L}$  uses  $\hat{\mathbf{x}}_0$  as per equation (6), instead of  $\hat{\mathbf{x}}_0$ . The measured data only factors in through learning the LoRA injection.

SCD recovers the walnut reporting a PSNR of 26.67dB with 20 optimisation steps per iteration and a LoRA rank of 4, while SCD omitting line 7, still shows comparable results, but requires 60 optimisation step per iteration (instead of 20), and a LoRA rank of 32 (instead of 4), introducing much unnecessary computational overhead. Adapting with respect to the conditioned Tweedie estimate for  $\mathbb{E}[\mathbf{x}_0|\mathbf{x}_t, \mathbf{y}]$  can thus be seen as a warm-starting of the optimisation of the LoRA injection. In variational regularisation, the data-fit term is augmented with a regularisation functional; see eq. (2). The role of the regulariser in eq. (9) is investigated as well, as an ablation study, reported in Appendix B. While all our experiments using CT include TV as regulariser in eq. (9), we find that the regularization has minor effects.

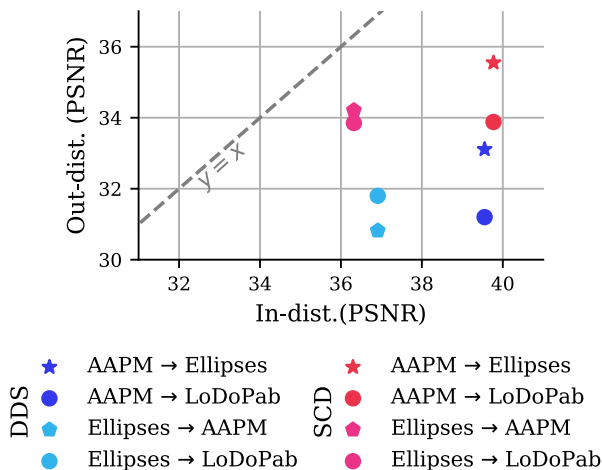


Figure 5: Comparison of DDS (Chung, Lee, and Ye 2023) vs. SCD on several in-distribution vs. out-of-distribution datasets for CT. The legend describes the PSNR on In-dist. data  $\rightarrow$  Out-dist. data.

### Boosting OOD robustness in Medical CT and MRI

SCD is evaluated against DDS on OOD reconstructive tasks from simulated sparse-view CT data, accelerated multi-coil MRI data, and a novel real-measured MDCT of a pig, used for volumetric SR. For sparse-view CT the data is simulated based on ground truth images from the AAPM, ELLIPSES and LODOPAB datasets, cf. Section 4. PSNR/SSIM values are reported in Table 1, with SCD consistently outperforming DDS across all CT tasks, leading to a 2 to 4dB higher PSNR. Figure 2 shows that to improved PSNR/SSIM values, qualitatively visual improvements can also be observed. Figure 5 shows that SCD is able to improve OOD performance on the sparse-view CT setting. It is worth noting that even in the in-distribution setting, i.e.,  $q(\mathbf{x}_0) = \tilde{q}(\mathbf{x}_0)$ , minor improvements are still observed, since SCD introduced the LoRA injection specific for each reconstruction.

Analogously, Table 1 shows that SCD improves DDS on OOD reconstructive settings. Adapting from BRAIN to KNEE requires capturing high-frequency image features, which are not present in BRAIN. Figure 3 shows example

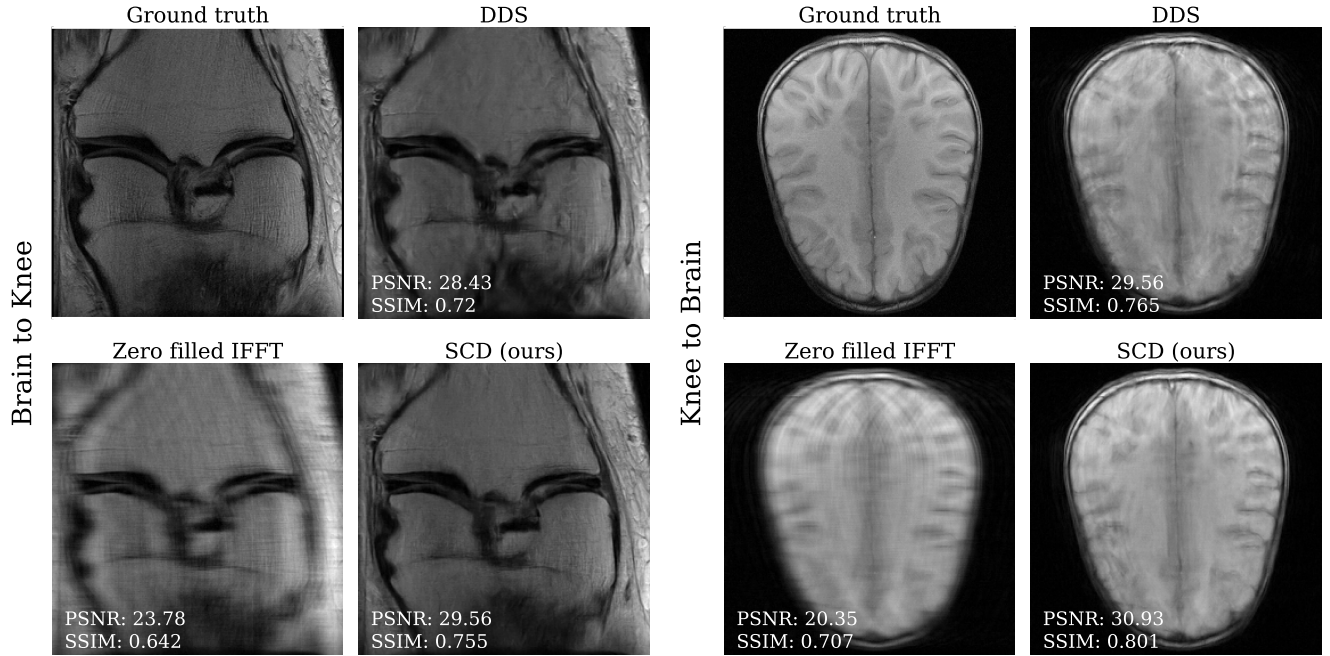


Figure 3: Results for accelerated MRI. We test two settings: training on BRAIN and testing on KNEE, and training on KNEE and testing on BRAIN. As a classical baseline, we also show the zero filled IFFT reconstruction.

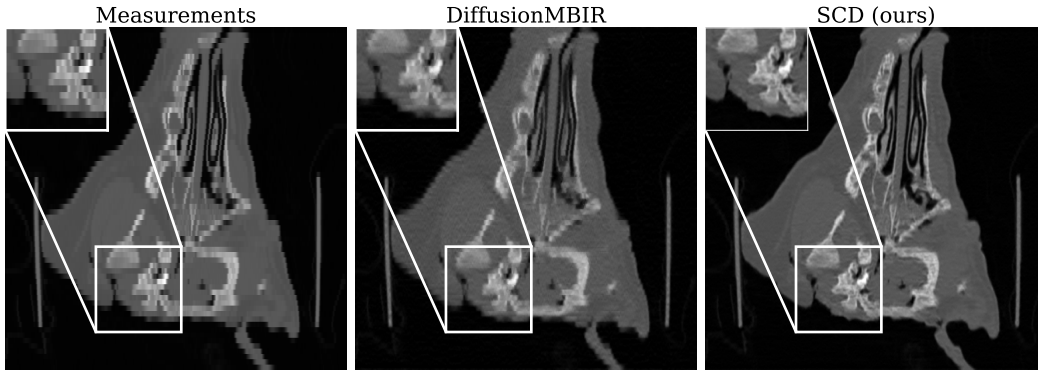


Figure 4: Coronal slice for SR. Axial and coronal views are shown in Appendix A.

reconstructions. Although the performance gains in terms of PSNR/SSIM are not as significant as for CT, we can observe that DDS introduces hallucinations in the reconstruction, which can be resolved using SCD.

For the volumetric SR task, we use a different baseline compared to DDS. We benchmark against DiffusionMBIR (Chung et al. 2023b), which is a framework to apply pre-trained 2D diffusion models for 3D reconstruction. Figure 4 shows the results on SR, where SCD greatly outperforms DiffusionMBIR. Here, we only provide a qualitative analysis as there is no available ground truth image.

## 6 Conclusion

In this work, we introduce Steerable Conditional Diffusion, a method that adapts diffusion models during reverse sampling, relying solely on a single measured data. Our experiments across diverse imaging modalities reveal that when applied to OOD reconstruction tasks, diffusion models can generate hallucinatory features from the training dataset. Through the proposed approach, we demonstrate that adapting diffusion models drastically mitigates these artefacts. Furthermore, we showcase that the LoRA approach not only provides a memory-efficient fine-tuning solution but is also applicable to diffusion models in reverse sampling for solving imaging inverse problems. As future research, extending our approach to scenarios involving a more extensive collec-

tion of measured data holds promise.

## Acknowledgements

The authors would like to thank Johannes Leuschner for fruitful discussions. R.B. acknowledges support from the i4health PhD studentship (UK EPSRC EP/S021930/1). A.D. acknowledges support from the Deutsche Forschungsgemeinschaft (DFG, German Research Foundation) - Project number 281474342/GRK2224/2. B.J. and S.A. acknowledge support from UK EPSRC grants EP/T000864/1 and EP/V026259/1. P.M. acknowledges support from DFG-NSFC project M-0187 of the Sino-German Center mobility programme. H.C. and J.C.Y. acknowledge support from the National Research Foundation of Korea under the Grant NRF-2020R1A2B5B03001980.

## References

- Abu-Hussein, S.; Tirer, T.; and Giryes, R. 2022. Adir: Adaptive diffusion for image reconstruction. *arXiv preprint arXiv:2212.03221*.
- Adler, J.; Kohr, H.; and Öktem, O. 2017. ODL 0.6.0.
- Adler, J.; and Öktem, O. 2018. Learned primal-dual reconstruction. *IEEE transactions on medical imaging*, 37(6): 1322–1332.
- Antun, V.; Renna, F.; Poon, C.; Adcock, B.; and Hansen, A. C. 2020. On instabilities of deep learning in image reconstruction and the potential costs of AI. *Proceedings of the National Academy of Sciences*, 117(48): 30088–30095.
- Arridge, S.; Maass, P.; Öktem, O.; and Schönlieb, C.-B. 2019. Solving inverse problems using data-driven models. *Acta Numer.*, 28: 1–174.
- Baguer, D. O.; Leuschner, J.; and Schmidt, M. 2020. Computed tomography reconstruction using deep image prior and learned reconstruction methods. *Inverse Problems*, 36(9): 094004.
- Barbano, R.; Leuschner, J.; Schmidt, M.; Denker, A.; Hauptmann, A.; Maass, P.; and Jin, B. 2022. An Educated Warm Start for Deep Image Prior-Based Micro CT Reconstruction. *IEEE Trans. Computational Imaging*, 8: 1210–1222.
- Chung, H.; Kim, J.; McCann, M. T.; Klasky, M. L.; and Ye, J. C. 2023a. Diffusion Posterior Sampling for General Noisy Inverse Problems. In *The Eleventh International Conference on Learning Representations, ICLR 2023, Kigali, Rwanda, May 1-5, 2023*.
- Chung, H.; Kim, J.; and Ye, J. C. 2023. Direct Diffusion Bridge using Data Consistency for Inverse Problems. *arXiv preprint arXiv:2305.19809*.
- Chung, H.; Lee, S.; and Ye, J. C. 2023. Fast Diffusion Sampler for Inverse Problems by Geometric Decomposition. *arXiv preprint arXiv:2303.05754*.
- Chung, H.; Ryu, D.; McCann, M. T.; Klasky, M. L.; and Ye, J. C. 2023b. Solving 3d inverse problems using pre-trained 2d diffusion models. In *Proceedings of the IEEE/CVF Conference on Computer Vision and Pattern Recognition*, 22542–22551.
- Chung, H.; Sim, B.; Ryu, D.; and Ye, J. C. 2022. Improving diffusion models for inverse problems using manifold constraints. *Advances in Neural Information Processing Systems*, 35: 25683–25696.
- Chung, H.; and Ye, J. C. 2022. Score-based diffusion models for accelerated MRI. *Medical image analysis*, 80: 102479.
- Daras, G.; Shah, K.; Dagan, Y.; Gollakota, A.; Dimakis, A. G.; and Klivans, A. 2023. Ambient Diffusion: Learning Clean Distributions from Corrupted Data. *arXiv preprint arXiv:2305.19256*.
- Der Sarkissian, H.; Lucka, F.; van Eijnatten, M.; Colacicco, G.; Coban, S. B.; and Batenburg, K. J. 2019. A cone-beam X-ray computed tomography data collection designed for machine learning. *Scientific data*, 6(1): 215.
- Dhariwal, P.; and Nichol, A. 2021. Diffusion models beat gans on image synthesis. *Advances in Neural Information Processing Systems*, 34: 8780–8794.
- Dimakis, A. G. 2022. *Deep Generative Models and Inverse Problems*, 400–421. Cambridge University Press.
- Du, Y.; Durkan, C.; Strudel, R.; Tenenbaum, J. B.; Dieleman, S.; Fergus, R.; Sohl-Dickstein, J.; Doucet, A.; and Grathwohl, W. 2023. Reduce, Reuse, Recycle: Compositional Generation with Energy-Based Diffusion Models and MCMC. *arXiv preprint arXiv:2302.11552*.
- Efron, B. 2011. Tweedie’s formula and selection bias. *Journal of the American Statistical Association*, 106(496): 1602–1614.
- Ho, J.; Jain, A.; and Abbeel, P. 2020. Denoising diffusion probabilistic models. *Advances in neural information processing systems*, 33: 6840–6851.
- Hu, E. J.; Shen, Y.; Wallis, P.; Allen-Zhu, Z.; Li, Y.; Wang, S.; Wang, L.; and Chen, W. 2022. LoRA: Low-Rank Adaptation of Large Language Models. In *The Tenth International Conference on Learning Representations, ICLR 2022, Virtual Event, April 25-29, 2022*.
- Jalal, A.; Arvinte, M.; Daras, G.; Price, E.; Dimakis, A. G.; and Tamir, J. 2021. Robust compressed sensing mri with deep generative priors. *Advances in Neural Information Processing Systems*, 34: 14938–14954.
- Kalra, M. K.; Maher, M. M.; D’Souza, R.; and Saini, S. 2004. Multidetector computed tomography technology: current status and emerging developments. *Journal of computer assisted tomography*, 28: S2–S6.
- Kang, E.; Min, J.; and Ye, J. C. 2017. A deep convolutional neural network using directional wavelets for low-dose X-ray CT reconstruction. *Medical physics*, 44(10): e360–e375.
- Kawar, B.; Elata, N.; Michaeli, T.; and Elad, M. 2023. GSURE-Based Diffusion Model Training with Corrupted Data. *arXiv preprint arXiv:2305.13128*.
- Kim, K.; and Ye, J. C. 2021. Noise2score: tweedie’s approach to self-supervised image denoising without clean images. *Advances in Neural Information Processing Systems*, 34: 864–874.
- Kingma, D. P.; and Ba, J. 2015. Adam: A Method for Stochastic Optimization. In Bengio, Y.; and LeCun, Y., eds., *3rd International Conference on Learning Representations*,

- ICLR 2015, San Diego, CA, USA, May 7-9, 2015, Conference Track Proceedings.
- Leuschner, J.; Schmidt, M.; Baguer, D. O.; and Maass, P. 2021. LoDoPaB-CT, a benchmark dataset for low-dose computed tomography reconstruction. *Scientific Data*, 8(1): 109.
- Liu, G.; Sun, H.; Li, J.; Yin, F.; and Yang, Y. 2023. Accelerating Diffusion Models for Inverse Problems through Shortcut Sampling. *arXiv preprint arXiv:2305.16965*.
- Moen, T. R.; Chen, B.; Holmes III, D. R.; Duan, X.; Yu, Z.; Yu, L.; Leng, S.; Fletcher, J. G.; and McCollough, C. H. 2021. Low-dose CT image and projection dataset. *Medical physics*, 48(2): 902–911.
- Natterer, F. 2001. *The mathematics of computerized tomography*. SIAM.
- Natterer, F.; and Wübbeling, F. 2001. *Mathematical methods in image reconstruction*, volume 5 of *SIAM monographs on mathematical modeling and computation*. SIAM. ISBN 978-0-89871-472-2.
- Poole, B.; Jain, A.; Barron, J. T.; and Mildenhall, B. 2023. DreamFusion: Text-to-3D using 2D Diffusion. In *The Eleventh International Conference on Learning Representations, ICLR 2023, Kigali, Rwanda, May 1-5, 2023*.
- Ravula, S.; Levac, B.; Jalal, A.; Tamir, J. I.; and Dimakis, A. G. 2023. Optimizing Sampling Patterns for Compressed Sensing MRI with Diffusion Generative Models. *arXiv preprint arXiv:2306.03284*.
- Rudin, L. I.; Osher, S.; and Fatemi, E. 1992. Nonlinear total variation based noise removal algorithms. *Physica D: non-linear phenomena*, 60(1-4): 259–268.
- Salimans, T.; and Ho, J. 2021. Should EBMs model the energy or the score? In *Energy Based Models Workshop-ICLR 2021*.
- Sohl-Dickstein, J.; Weiss, E.; Maheswaranathan, N.; and Ganguli, S. 2015. Deep unsupervised learning using nonequilibrium thermodynamics. In *International conference on machine learning*, 2256–2265. PMLR.
- Song, J.; Meng, C.; and Ermon, S. 2021. Denoising Diffusion Implicit Models. In *9th International Conference on Learning Representations, ICLR 2021, Virtual Event, Austria, May 3-7, 2021*.
- Song, Y.; Sohl-Dickstein, J.; Kingma, D. P.; Kumar, A.; Ermon, S.; and Poole, B. 2020. Score-based generative modeling through stochastic differential equations. *arXiv preprint arXiv:2011.13456*.
- Tran, D.; Snoek, J.; and Lakshminarayanan, B. 2020. Practical uncertainty estimation and out-of-distribution robustness in deep learning. *Technical report, Google Brain*.
- Uecker, M.; Lai, P.; Murphy, M. J.; Virtue, P.; Elad, M.; Pauly, J. M.; Vasanawala, S. S.; and Lustig, M. 2014. ESPIRiT—an eigenvalue approach to autocalibrating parallel MRI: where SENSE meets GRAPPA. *Magnetic resonance in medicine*, 71(3): 990–1001.
- Ulyanov, D.; Vedaldi, A.; and Lempitsky, V. 2018. Deep image prior. In *Proceedings of the IEEE conference on computer vision and pattern recognition*, 9446–9454.
- Wang, G.; Ye, J. C.; and Man, B. D. 2020. Deep learning for tomographic image reconstruction. *Nat. Mach. Intell.*, 2(12): 737–748.
- Wu, L.; Trippe, B. L.; Naesseth, C. A.; Blei, D. M.; and Cunningham, J. P. 2023. Practical and Asymptotically Exact Conditional Sampling in Diffusion Models. *arXiv preprint arXiv:2306.17775*.
- Zbontar, J.; Knoll, F.; Sriram, A.; Murrell, T.; Huang, Z.; Muckley, M. J.; Defazio, A.; Stern, R.; Johnson, P.; Bruno, M.; et al. 2018. fastMRI: An open dataset and benchmarks for accelerated MRI. *arXiv preprint arXiv:1811.08839*.
- Zhao, Z.; Ye, J. C.; and Bresler, Y. 2023. Generative Models for Inverse Imaging Problems: From mathematical foundations to physics-driven applications. *IEEE Signal Process. Mag.*, 40(1): 148–163.

## A Additional Experimental Material

### Datasets

**AAPM** We train a model on the dataset of abdominal CT scans released by the American Association of Physicists in Medicine (AAPM) for the 2016 grand challenge. We transform the data according to (Kang, Min, and Ye 2017) to match the training setting of (Chung et al. 2022). The AAPM dataset consists of 3839 training images resized to  $256 \times 256$  pixels. We construct a held-out validation set comprising 10 slices, used for the hyperparameter search, and a held-out test set comprising 56 images (equidistant with respect to the  $z$ -axis) to compute performance image metrics. We simulate measurements according to a parallel beam geometry using 60 angles, using ODL (Adler, Kohr, and Öktem 2017), and adding 1% relative Gaussian noise.

**LoDoPab Dataset (Leuschner et al. 2021)** The LODOPAB dataset contains human chest CT scans. We resize the LODOPAB test set to  $256 \times 256$  px and rotate each slice to match the anatomical orientation in AAPM. Analogously, we construct a held-out validation set (out of the test set) comprising 10 slices, used for the hyperparameter search. Additionally, 100 slices are taken from the LODOPAB test set to compute performance image metrics. For the simulation of the data measurements, we follow the same setting as in AAPM.

**Ellipses (Adler and Öktem 2018)** We train a diffusion model on a synthetic dataset containing images of a varying number of ellipses with random orientations and sizes. The simulation of this dataset follows the same setting as the one used in (Barbano et al. 2022). In particular, we generate 32000 images on-the-fly. The use of synthetic data for training is particularly useful in imaging domain where obtaining large-scale datasets is infeasible or expensive.

**$\mu$ CT Walnut (Der Sarkissian et al. 2019)** The  $\mu$ CT WALNUT dataset consists of cone-beam projection data and high-quality reconstructions of  $501 \times 501$  px. We use the operator provided by (Barbano et al. 2022), which is a sparse-matrix operator released by the authors to reconstruct the middle-slice from the publicly available measured data.

In particular, the operator sup-samples to 120 detector pixels and 60 angles in order to solve a sparse-view CT inverse problem. Since our models are trained on a image resolution of  $256 \times 256$  px, we also apply an up-sampling operator to the inverse problem. The reconstruction task then becomes recovering  $\mathbf{x}$ , which has the same dimensionality of the output of our model, i.e.  $256 \times 256$  px, from the measured data  $\mathbf{y}$ ,

$$\mathbf{y} = A(S(\mathbf{x})),$$

where  $S$  describes nearest-neighbour up-sampling to  $501 \times 501$  px and  $A$  is the sparse-view CT operator.

**FastMRI (Zbontar et al. 2018)** The FastMRI datasets include data from both clinical KNEE and BRAIN MRI scans. The model trained on KNEE used 29877 slices from 973 volumes for training. The model trained on BRAIN used 83216 slices from 3842 volumes for training. We drop

the first/last 5 slices from each volume as they mostly contain noise. The evaluation was done using 236 slices from 18 test volumes for BRAIN and 294 slices from 10 test volumes for KNEE.

**$\mu$ CT Pig** A domestic pig (*Sus scrofa domestica*) head was prepared for  $\mu$ CT scanning. The specimen was firmly positioned on the  $\mu$ CT scanner’s holder to ensure stability throughout the scan. Imaging was conducted using the Skyscan 1273  $\mu$ CT scanner (Bruker, Kontich, Belgium). A resolution of  $100 \mu\text{m}$  was chosen based on the specimen’s dimensions and imaging needs. The tube voltage was set at 125 kV, with a tube current of  $300 \mu\text{A}$ . A rotation step of  $0.3^\circ$  was selected for optimal image capture, with a scanning position of 112 mm. The scan lasted approximately 30 minutes, capturing 689 projections. Image reconstruction was performed using the Skyscan NRecon software, and the images were adjusted to enhance visualisation of the specimen’s internal structures. The resulting images had a resolution of  $768 \times 768$  px. As our training data we used the  $512 \times 512$  px center crop from 3768 slices. Example images from the training dataset are shown in Figure 6. For the OOD experiments 5mm coarse-vertical-resolution scans of pig heads were performed. The pig was laid supine on the CT table, with their head stabilised in a neutral position using a head holder. Imaging was performed using either the Siemens Somatom Force (Siemens Healthineers, Erlangen, Germany) or the Canon Aquilion One (Canon Medical Systems, Otawara, Tochigi, Japan) CT scanner. The tube voltage ranged from 100 to 120 kV, and the tube current was adjusted between 125 and 330 mA. A medium field of view (FOV) was selected to cover the entire brain, reducing peripheral artefacts. Images were reconstructed using a standard soft tissue algorithm. The reconstruction problem is formulated as a  $\times 8$  SR in the  $z$ -direction. We apply our SCD independently to each coronal slice to create the full volumetric reconstruction.

### Experimental Details

For all our experiments, we tune the hyperparameters of DDS and SCD by running a sweep over parameter values, and comparing the performance on the validation set. The hyperparameters with the best performance on the validation set, with respect to the PSNR, are used to evaluate the performance on the test set. The best hyperparameters for both SCD and DDS are shown in Table 3 and 4, respectively.

For our sparse view CT setting, we choose the total variation (TV) as the additional regulariser for the adaptation, i.e.,  $\mathcal{R}(\mathbf{x}) = \text{TV}(\mathbf{x})$  (Rudin, Osher, and Fatemi 1992), and we make use of the PyTorch automatic differentiation framework for optimisation.

### Training Details

For all of our experiments we used the Attention U-Net architecture used in (Dhariwal and Nichol 2021) available at <https://github.com/openai/guided-diffusion>. This network architecture has a U-Net backbone, and a time-step encoding. We use the LoRA reparametrisation for the U-Net, i.e.,

Example images  $\mu$ CT

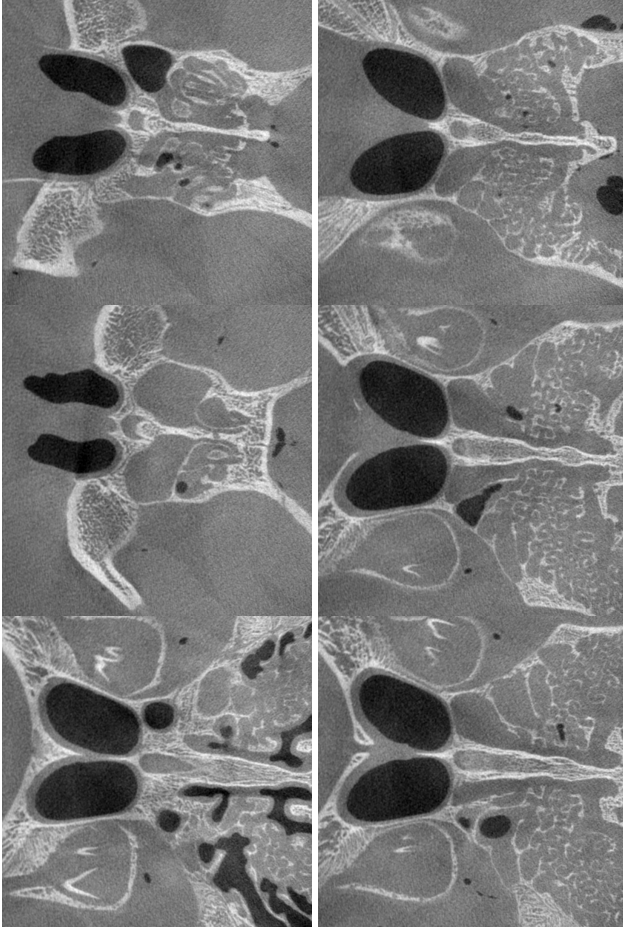


Figure 6: Example images of the  $\mu$ CT training dataset used for SR.

all attention and convolutional layers. Additionally, we re-train all biases in the U-Net as in (Hu et al. 2022), since the biases only account for a negligible number of parameters. Note that the time-step encoding is not changed at all during the fine-tuning process. We trained each network for 1M steps.

## B Additional Results

### Ablation Study: Without Regularisation in eq. (9)

In this ablation, we want to study the influence of the additional TV regulariser for the adaptation objective in eq. (9). We do this for sparse-view CT experiments. We follow the same experimental setting as the sparse-view CT experiments, presented in Table 1. However, the increase in performance in most settings is only marginal.

$q(\mathbf{x}_0)$	$\tilde{q}(\mathbf{x}_0)$	SCD	
		PSNR	SSIM
AAPM	AAPM	39.73 $\pm$ 0.07	0.952 $\pm$ 0.001
	LODOPAB	34.21 $\pm$ 0.25	0.850 $\pm$ 0.008
	ELLIPSES	35.41 $\pm$ 0.10	0.954 $\pm$ 0.001
ELLIPSES	ELLIPSES	36.02 $\pm$ 0.08	0.968 $\pm$ 0.000
	AAPM	33.98 $\pm$ 0.12	0.883 $\pm$ 0.002
	LODOPAB	33.42 $\pm$ 0.25	0.829 $\pm$ 0.008

Table 2: PSNR and SSIM (mean  $\pm$  SE) for SCD without the additional TV regulariser.

## C On the Likelihood Approximation

In this section, we want to take a closer look on the approximation to the gradient of the likelihood. In our work, we propose to approximate the gradient as

$$\begin{aligned} \nabla_{\mathbf{x}}[\log p(\mathbf{y}|\cdot)](\mathbf{x}_t) &\approx -\frac{1}{2\sigma_y^2(1-\bar{\alpha}_t)} \nabla_{\mathbf{x}}[\|\mathbf{A}\hat{\mathbf{x}}_0 - \mathbf{y}\|_2^2](\mathbf{x}_t) \\ &\approx -\frac{\sqrt{\bar{\alpha}_t}}{2\sigma_y^2(1-\bar{\alpha}_t)} \nabla_{\mathbf{x}}[\|\mathbf{A}\hat{\mathbf{x}}_0 - \mathbf{y}\|_2^2](\hat{\mathbf{x}}_0). \end{aligned}$$

with  $\frac{\sqrt{\bar{\alpha}_t}}{\sigma_y^2(1-\bar{\alpha}_t)}$  being our designed step-size. Note that the time-dependent likelihood is defined by

$$p(\mathbf{y}|\mathbf{x}_t) = \int p(\mathbf{y}|\mathbf{x}_0)p(\mathbf{x}_0|\mathbf{x}_t)d\mathbf{x}_0, \quad (10)$$

and requires to be approximated. The first approximation is given in (Chung et al. 2023a),

$$p(\mathbf{y}|\mathbf{x}_t) \approx p(\mathbf{y}|\mathbb{E}[\mathbf{x}_0|\mathbf{x}_t]), \quad (11)$$

and approximate the conditional mean using Tweedie’s formula:

$$\mathbb{E}[\mathbf{x}_0|\mathbf{x}_t] \approx \hat{\mathbf{x}}_0(\mathbf{x}_t) := (\mathbf{x}_t - \sqrt{1-\bar{\alpha}_t}\epsilon(\mathbf{x}_t, t; \boldsymbol{\theta}^*)) / \sqrt{\bar{\alpha}_t}$$

Using the Gaussian noise model, we recover the first approximation

$$\nabla_{\mathbf{x}}[\log p(\mathbf{y}|\cdot)](\mathbf{x}_t) \propto -1/2 \nabla_{\mathbf{x}}[\|\mathbf{A}\hat{\mathbf{x}}_0 - \mathbf{y}\|_2^2](\mathbf{x}_t)$$

where we differentiate w.r.t.  $\mathbf{x}_t$ , i.e., we have to back-propagate through the score model

$$\mathbf{A}^\top(\mathbf{y} - \mathbf{A}\hat{\mathbf{x}}_0).$$

We can now calculate the Jacobian of Tweedie w.r.t  $\mathbf{x}_t$

$$\partial_{\mathbf{x}_t} \hat{\mathbf{x}}_0 \approx 1/\sqrt{\bar{\alpha}_t} (I_{d_x} - \sqrt{1-\bar{\alpha}_t} \partial_{\mathbf{x}_t} \epsilon(\mathbf{x}_t, t; \boldsymbol{\theta}^*)),$$

where  $\partial_{\mathbf{x}_t} \epsilon(\mathbf{x}_t, t; \boldsymbol{\theta}^*) \in \mathbb{R}^{d_x \times d_x}$ . The gradient of the score model is often unstable, so we follow (Poole et al. 2023) and approximate it with a scaled identity

$$\partial_{\mathbf{x}_t} \epsilon(\mathbf{x}_t, t; \boldsymbol{\theta}^*) \approx \sqrt{1-\bar{\alpha}_t} I_{d_x}.$$

Note, that  $\sqrt{1-\bar{\alpha}_t}$  is the standard variation of the noise in  $\mathbf{x}_t$ . Thus we get

$$\partial_{\mathbf{x}_t} \hat{\mathbf{x}}_0 \approx 1/\sqrt{\bar{\alpha}_t} (I_{d_x} - (1-\bar{\alpha}_t)I_{d_x}) = \sqrt{\bar{\alpha}_t} I_{d_x}.$$

Using this approximation we get

$$-1/2 \nabla_{\mathbf{x}}[\|\mathbf{A}\hat{\mathbf{x}}_0 - \mathbf{y}\|_2^2](\mathbf{x}_t) \approx -\sqrt{\bar{\alpha}_t} \mathbf{A}^\top(\mathbf{y} - \mathbf{A}\hat{\mathbf{x}}_0).$$

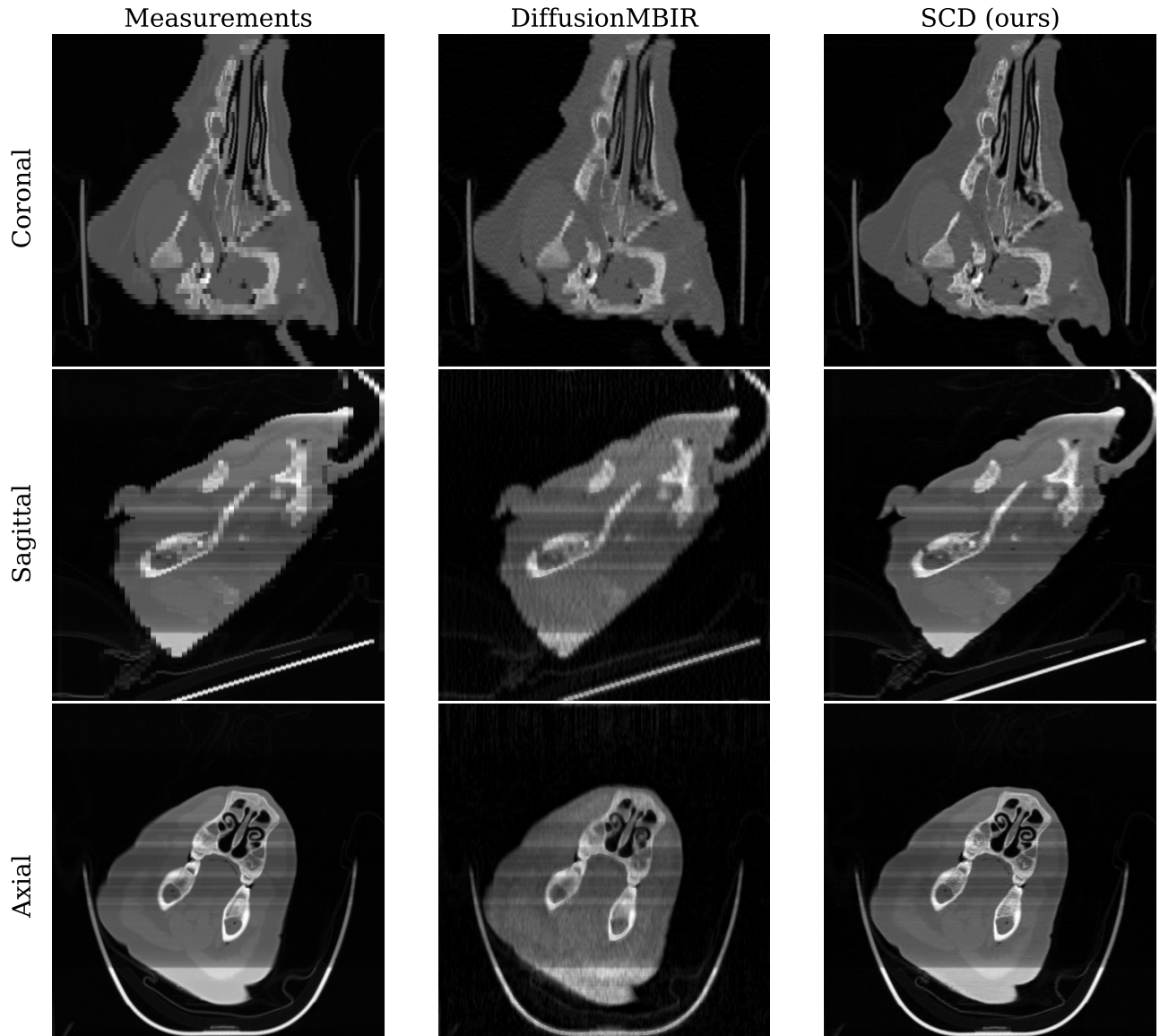


Figure 7: Additional results for SR. We show sagittal, coronal and axial slices of the  $\mu$ CT of a pig head. Note that the SR is performed with respect to the  $z$ -axis. The axial slice was scanned in full resolution, i.e., the forward operator is the identity in this direction.

$q(\mathbf{x}_0)$	$\tilde{q}(\mathbf{x}_0)$	$\lambda$	optim. steps	lr.	$\gamma$	LoRA rank	sampl. steps	cg iter
AAPM	AAPM	1e-5	3	1e-4	10	4	50	1
	LODOPAB	5e-5	10	1e-3	10	4	50	1
	ELLIPSES	5e-6	10	1e-3	0.1	4	50	1
	WALNUT	1e-5	5	1e-3	10	4	50	1
ELLIPSES	ELLIPSES	1e-5	4	1e-4	10	4	50	12
	AAPM	1e-5	25	1e-3	1	30	50	1
	LODOPAB	1e-5	25	1e-3	1	30	50	1
	WALNUT	5e-6	20	1e-3	1	4	75	1
KNEE	KNEE	n/a	3	1e-3	5	4	50	3
	BRAIN	n/a	3	1e-3	5	4	50	3
BRAIN	BRAIN	n/a	3	1e-3	5	4	50	3
	KNEE	n/a	3	1e-3	5	4	50	3

Table 3: Hyperparameters for SCD.

$q(\mathbf{x}_0)$	$\tilde{q}(\mathbf{x}_0)$	$\gamma$	sampl. steps	cg iter	$\eta$
AAPM	AAPM	0.1	50	2	0.85
	LODOPAB	0.1	50	5	0.85
	ELLIPSES	0.1	100	10	0.85
	WALNUT	0.1	75	2	0.85
ELLIPSES	ELLIPSES	10	100	12	0.75
	AAPM	0.01	50	15	0.85
	LODOPAB	0.1	50	10	0.95
	WALNUT	10	50	3.0	0.95
KNEE	KNEE	5	50	3	0.85
	BRAIN	5	50	3	0.85
KNEE	KNEE	5	50	3	0.85
	BRAIN	5	50	3	0.85

Table 4: Hyperparameters for DDS.